Wrap-Around Wearable Coils for Seamless Monitoring of Joint Flexion

Vigyanshu Mishra, *Student Member, IEEE* and Asimina Kiourti, *Member, IEEE*

Abstract*— *Objective: **We introduce and validate a new class of wearable coils that seamlessly monitor joint flexion in the individual's natural environment while overcoming shortcomings in the state-of-the-art.** ***Methods:*** **Our approach relies on Faraday's Law of Induction and employs wrap-around transmit and receive coils that get angularly misaligned as the joint flexes.** ***Results:*** **Simulation and *in vitro* measurement results for both copper and e-thread coils are in excellent agreement. As a proof-of-concept, a cylindrical arm model is considered and feasibility of monitoring the 0^o to 130^o range of motion is confirmed. The operation frequency of 34 MHz is identified as optimal, bringing forward reduced power requirements, enhanced angular resolution, and extreme robustness to tissue dielectric property variations. Performance benchmarking vs. state-of-the-art inertial measurement units shows equivalent or superior performance, particularly for flexion angles greater than 20^o. Design guidelines and safety considerations are also explored.** ***Conclusion:*** **Contrary to "gold-standard" camera-based motion capture, the reported approach is not restricted to contrived environments. Concurrently, it does not suffer from integration drift (unlike inertial measurement units), it does not require line-of-sight (unlike time-of-flight sensors), and it does not restrict natural joint movement (unlike bending sensors).** ***Significance:*** **The reported approach is envisioned to be seamlessly integrated into garments and, eventually, redefine the way joint flexion is monitored at present. This promises unprecedented opportunities for rehabilitation, sports, gestural interaction, and more.**

***Index Terms*— Body kinematics, coils, e-textiles, inductive coupling, joint flexion, wearables.**

I. Introduction

JOINT flexion is an intrinsic part of human motion, with different body parts relying on flexion/extension of different joints (elbow, knee, and so on) to perform activities as diverse as walking, running, climbing, etc. Expectedly, the feasibility of monitoring joint flexion as a function of time opens doors for numerous applications that include, but are not limited to: (a) healthcare (e.g., rehabilitation progress monitoring) [1], [2] (b) sports (e.g., personalized training) [3], [4], (c) gestural recognition (e.g., human-computer interfaces) [5], [6], and (d) consumer electronics (e.g., gaming) [7], [8].

TABLE I
Comparison of Approaches for Monitoring Joint Flexion

	Camera-based	IMUs	Time-of-Flight	Bending Sensors	Proposed
Works in real-world settings	No (-)	Yes (+)	Yes (+)	Yes (+)	Yes (+)
Seamless	Yes (+)	No (-)	No (-)	Yes (+)	Yes (+)
Insensitive to Line-of-Sight	No (-)	Yes (+)	No (-)	Yes (+)	Yes (+)
Allows natural motion	Yes (+)	Yes (+)	Yes (+)	No (-)	Yes (+)
Reliable vs. time	Yes (+)	No (-)	Yes (+)	Yes (+)	Yes (+)
3D motion capture	Yes (+)	Yes (+)	Yes (+)	Flexion only	Flexion only

To date, a number of technologies have been reported for monitoring joint flexion. Referring to Table I, the "gold standard" approach employs camera-based techniques, viz. optical/infrared cameras that track on-body retro-reflective markers [9], [10], or markerless techniques that use depth-sensitive cameras [11], [12]. These technologies are highly accurate but are restricted to contrived (e.g., lab) environments. For real-world operation, Inertial Measurement Units (IMUs) have been reported that rely on combinations of accelerometers, gyroscopes and magnetometers [13]-[15]. Unfortunately, IMUs suffer from integration drift (error caused by integrating acceleration to derive position) [13], [16] and are obtrusive and not injury-safe (e.g., in case of fall [17], [18]). Ongoing research on IMUs is geared more toward improving their algorithms rather than the hardware [13]-[15]. As an alternative, time-of-flight sensors use body-worn ultrasonic [16] or ultra-wideband transceivers [19] and measure the time taken for transmission as a way to assess distance and, hence, movement. However, they require line-of-sight at all times and are obtrusive. Finally, bending sensors rely on strain produced upon their constituent material to monitor flexion [20], [21]. This strain can either be converted to equivalent change in resistance [20], or used on magnetostricitive materials to change permeability and, hence, inductance (Villari effect) [21]. They operate in non-contrived settings and do not require line-of-sight. However, they are placed atop the joint thereby restricting natural movement as they bend along with the joint, and raise concerns as to the maximum number of flexes they can withstand.

To address these shortcomings in the state-of-the-art, we herewith introduce a new class of coils that may monitor joint flexion in uncontrived environments while also being

Manuscript received September 25, 2018; revised December 20, 2018; accepted January 18, 2019. This work was supported in part by the National Science Foundation under Grant 1842531.

V. Mishra and A. Kiourti are with the ElectroScience Laboratory, Department of Electrical and Computer Engineering, The Ohio State University, Columbus, OH, 43212, USA (e-mails: mishra.186@osu.edu, kiourti.1@osu.edu).

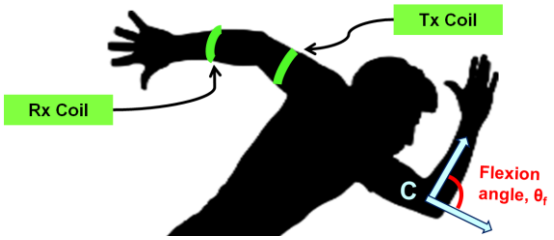

Fig. 1. Proposed wrap-around coils for monitoring joint flexion.

seamless, insensitive to line-of-sight, and reliable over time, Table I. By realizing such coils on e-threads, readily integration into daily garments [22]-[25] (shirts, leggings, etc.) is envisioned for monitoring joint flexion on the go. Focus of this work is on monitoring joint flexion/extension, regardless of rotational joint movements. As shown in Fig. 1, our approach relies on Faraday's Law of Induction and employs wrap-around transmit and receive coils that get angularly misaligned as the joint flexes. To our knowledge, this is the first time that wrap-around coils and inductive coupling principles are explored for joint flexion monitoring. In this paper, we present the operating principle of these wrap-around coils, and demonstrate proof-of-concept results that lay the foundations for further future development and optimization. Simulation and *in vitro* experimental results are contrasted for both copper wire and e-thread coils. A cylindrical arm model is considered, though results can be readily generalized to other joints (e.g., knee). Selection of optimal operation frequency, design guidelines, safety considerations and performance benchmarking vs. state-of-the-art IMUs are also explored.

II. Operating Principle

As shown in Fig. 1, the proposed wrap-around coils for monitoring joint flexion consist of a minimum of two coils, viz. a transmitting (Tx) and a receiving (Rx) coil. Both coils are wrapped around the limb, positioned right above and below the joint, respectively. The Rx receives the signal transmitted by the Tx, quantified as the magnitude of the transmission coefficient between the two ($|S_{21}|$). Depending on the frequency of operation, the same two coils may operate in different modes. That is, the coils may behave as: (a) antennas (circumference ~ λ), (b) inductive coils (electrically small antennas) (circumference < 0.1λ), or (c) a combination of both (0.1λ < circumference < λ). In all cases, $|S_{21}|$ will change as the flexion angle changes. Here, the flexion angle (θ_f in Fig. 1) is formed between the axes of the upper arm and forearm, meeting at the center of the joint 'C'. Expectedly, the underlying operating principle will change for each mode. As will be discussed next, the inductive mode of operation is identified as optimal for joint flexion monitoring, with the transmission efficiency considerably improving for resonant coils. In this case, if a time-varying current flows through the Tx, it will generate a time-varying magnetic flux density passing through the Rx. This will induce a voltage on the Rx based on Faraday's Law of Induction [26]:

$$V_{Rx} = -\frac{d}{dt}\iint \boldsymbol{B_{Tx}} \cdot \widehat{\boldsymbol{n_{Rx}}}\, ds \qquad (1)$$

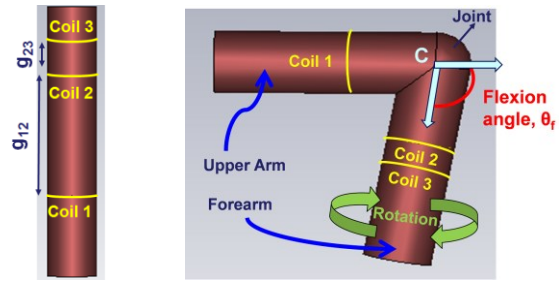

(a) (b)

Fig. 2. Simulation set-up showing: (a) extension, and (b) flexion of a cylindrical limb model.

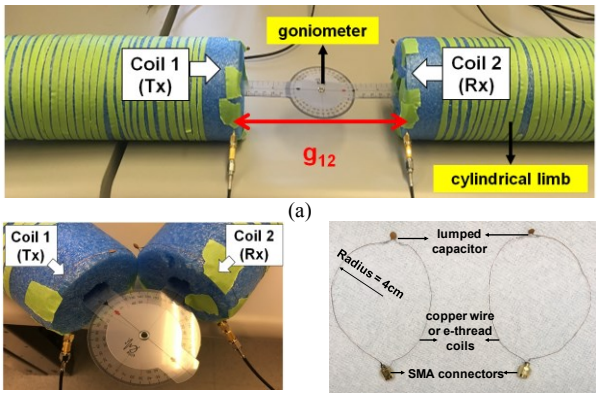

(a) (b) (c)

Fig. 3. Experimental set-up: (a) fully-extended model, (b) model flexed at $\theta_f = 100^o$, and (c) realization of resonant coils.

where, V_{Rx} is the voltage induced on the Rx, $\mathbf{B_{Tx}}$ is the magnetic flux density produced by the Tx, and $\widehat{\boldsymbol{n_{Rx}}}$ is the normal unit area vector of the Rx. As θ_f changes, $\widehat{\boldsymbol{n_{Rx}}}$ changes as well, altering the induced voltage V_{Rx}. That is, V_{Rx} changes as a function of θ_f. Equivalently, changes in V_{Rx} can be recorded to monitor θ_f and, hence, joint flexion.

III. Simulation and Experimental Set-Ups

A. Simulation Set-Up

The employed simulation set-up is shown in Fig. 2. As a proof-of-concept, a homogeneous cylindrical model of the human arm is considered. The upper arm and forearm are modeled as cylinders (3.9 cm in radius, 25 cm in length), while the elbow joint is modeled as a sphere (3.9 cm in radius). The tissue-simulating material is 2/3 muscle, as frequently used in the literature to represent the average human body properties [27], [28]. Two single-turn coils, Coil 1 (Tx per Fig. 1) and Coil 2 (Rx per Fig. 1) are wrapped around the cylindrical arm model, placed symmetrically with respect to the joint at a gap g_{12} between the two. Both coils exhibit a radius of 4 cm, are simulated with 30 AWG (0.254 mm-diameter) copper material, and are attached to a lumped capacitor to make them resonant. Optionally, a second receiving coil may be added to improve the system robustness and performance (Coil 3 in Fig. 2), as will be discussed in detail in Section VII.D. All simulations are carried out using the frequency-domain solver of the CST Microwave Studio®

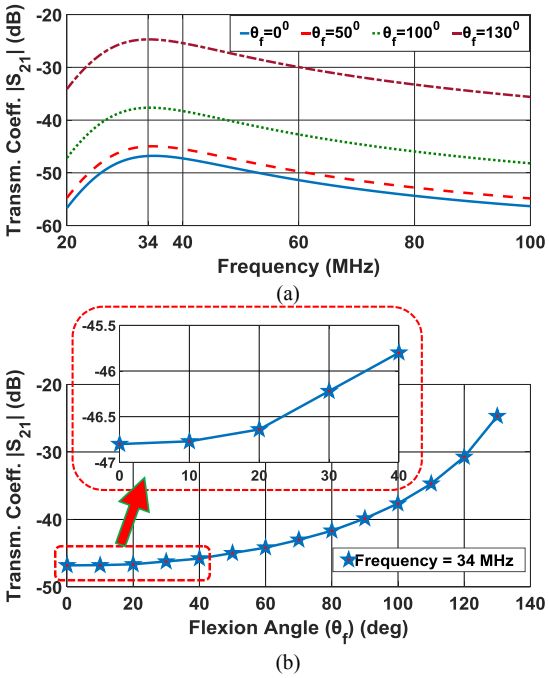

Fig. 4. Proof-of-concept simulation results for 34 MHz resonant coils: (a) $|S_{21}|$ as a function of frequency at different flexion angles, and (b) $|S_{21}|$ as a function of flexion angle (with zoomed in inset for $\theta_f = 0^0$ to 40^0).

and are based on the Finite Integral Technique. Tetrahedral mesh is used to discretize the computation domain.

B. Experimental Set-Up

The employed experimental set-up is shown in Fig. 3(a). The upper arm and forearm are realized using cylindrical Styrofoam ($\varepsilon_r \sim 1$), 4 cm in radius. The choice of material will become clear in Section V.A. In realizing this phantom, the key challenge lies in implementing a flexion mechanism that accurately emulates the arm's flexion/extension. This is achieved by fixing a goniometer inside the Styforoam to emulate the hinge motion. The latter also serves to measure the per case flexion angle (as reference). An example scenario where the joint is flexed by $\theta_f = 100^o$ is shown in Fig. 3(b).

Two types of coils are realized, viz. using rigid 30 AWG copper-wire and flexible 40-filament silver-based Liberator e-threads [29], respectively. In both implementations, the wire/e-thread diameter is equal to 0.254 mm, and a lumped capacitor is soldered to make the coils resonant, Fig. 3(c). The Tx (Coil 1) and Rx (Coil 2) are eventually connected to ports 1 and 2 of a PNA-L N5235A network analyzer that records $|S_{21}|$ as a function of flexion angle, θ_f.

IV. Proof-of-Concept Simulation Results

As a proof-of-concept, the simulation set-up of Fig. 2 is employed (Coils 1, 2 only) at an operation frequency of 34 MHz. This frequency falls in the inductive mode of operation, which will be shown in Section V to be the optimal mode. Lumped capacitors of 95.2 pF are attached to both coils to make them resonant at the intended frequency. To enable a 0^0 to 130^0 flexion range, the coil gap is set to g_{12} = 20 cm, per Fig. 2(a). Indeed, the 34 MHz resonance behavior is clearly

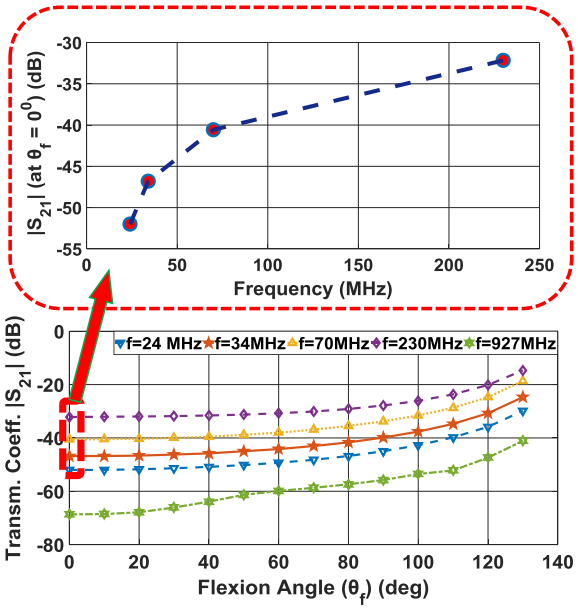

Fig. 5. $|S_{21}|$ as a function of flexion angle for various operating frequencies in the inductive, antenna, and combined modes.

visible in Fig. 4(a). Even more importantly, Fig. 4(a) shows that $|S_{21}|$ at resonance increases with an increase in flexion angle, θ_f. This is more evident in Fig. 4(b) that plots $|S_{21}|$ as a function of θ_f at resonance. Notably, there is a one-to-one correlation between $|S_{21}|$ and θ_f, confirming the feasibility of monitoring joint flexion via the proposed approach.

Simulations for non-resonant coils are also carried out, showing a similar trend to Fig. 4(b). Nevertheless, the values of $|S_{21}|$ are significantly lower in this case, e.g., $|S_{21}|$ is degraded by 7 dB at $\theta_f = 0^o$. That is, non-resonant coils can still be used for flexion monitoring, but the transmit power required to achieve a certain power level on the receive side will be much higher as compared to resonant coils. As such, resonant coils that are inherently capable of optimal power transfer are only considered in this study.

V. Selection of Optimal Operation Frequency

As mentioned in Section II, the same coils may operate in different modes (antenna, inductive, or combination of the two) depending on the selected operation frequency. Different modes have different advantages and disadvantages for monitoring joint flexion, implying a trade-off for optimal frequency selection. In particular, operating frequency is identified as having significant effect on mainly three parameters, i.e., a) power requirements, b) flexion angle resolution, and c) tissue dielectric property variations. A thorough study is hereafter presented that explores five representative frequencies (24, 34, 70, 230, and 927 MHz) with respect to the aforementioned parameters. To do so, the simulation set-up of Fig. 2 is considered (Coils 1, 2 only). Specifically, at frequencies below 120 MHz, coils of radius 4 cm operate in the inductive mode (circumference < 0.1λ). The 927 MHz frequency corresponds to the self-resonance of the coils where they behave as loop antennas, while 230 MHz

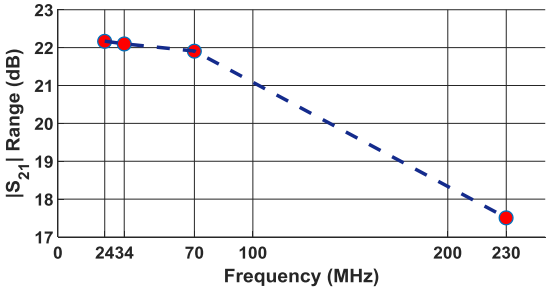

Fig. 6. Range of $|S_{21}|$ values calculated by subtracting $|S_{21}|$ at $\theta_f = 0^o$ from $|S_{21}|$ at $\theta_f = 130^o$, signifying the system resolution at different frequencies.

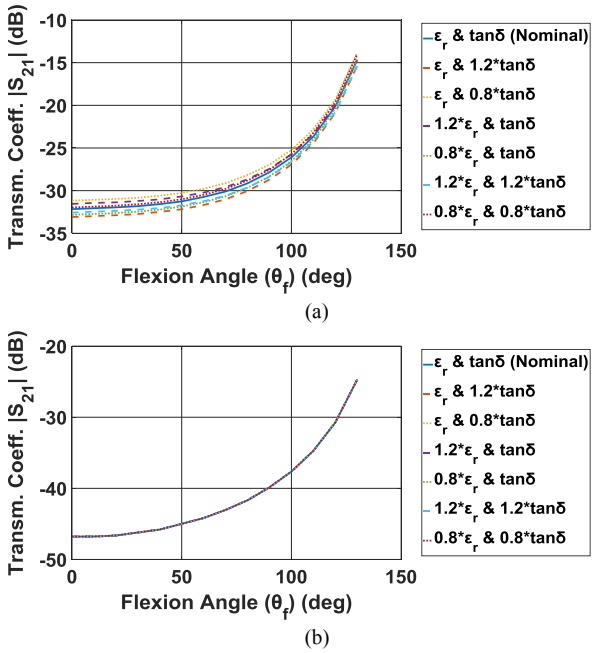

Fig. 7. Change in $|S_{21}|$ values with ±20% variation in tissue permittivity (ε_r) and loss tangent (tanδ) at (a) 230 MHz, and (b) 34 MHz. Nominal (εr & tanδ) values correspond to 2/3 muscle tissue properties.

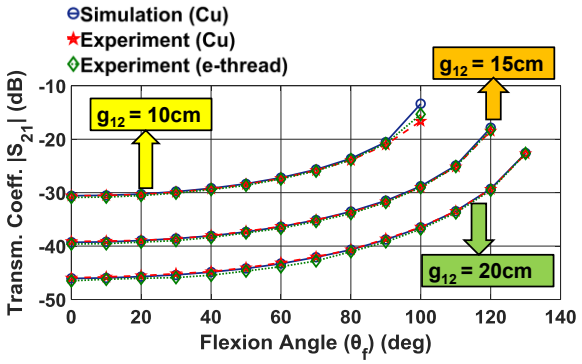

Fig. 8. Experimental vs. simulation results for copper and e-thread coils at 34 MHz.

corresponds to an example frequency in the combined mode of operation.

A. *Effect on Power Requirements*

Low transmit power is essential for minimizing battery requirements and ensuring conformance to safety standards [30]. Use of resonant coils improves transmission to a great extent (per Section IV), while optimal frequency selection may further boost transmission efficiency. To demonstrate the latter, Fig. 5 plots $|S_{21}|$ as a function of flexion angle (θ_f) at various operating frequencies. As seen, the antenna mode (927 MHz) does not show a one-to-one correlation between $|S_{21}|$ and θ_f, unlike the inductive and combined modes. Besides, the transmission coefficient, $|S_{21}|$, exhibits the lowest values for this mode making it the least efficient in terms of transmit power. With the above in mind, the antenna mode is considered unsuitable for the intended application. While in the inductive and combined modes, $|S_{21}|$ decreases as the operating frequency is reduced. This can be attributed to changes in impedance matching at different frequencies. Notably, this trend is not linear on the dB scale (see inset of Fig. 5), implying that transmission efficiency significantly reduces as we move down in frequency. That is, higher frequencies (in the inductive or combined mode) are preferred so as to enable higher received power levels or, equivalently, lower power requirements on the transmitter end.

B. *Effect on Flexion Angle Resolution*

As would be expected, high angular resolution is desired for the designed system, implying that the range of $|S_{21}|$ values corresponding to the extreme 0^o and 130^o flexion angles should be as large as possible. To better understand how this parameter is affected by the operating frequency, Fig. 6 plots the aforementioned $|S_{21}|$ range (i.e., $|S_{21}|$ at $\theta_f = 0^o$ subtracted from $|S_{21}|$ at $\theta_f = 130^o$) for operating frequencies in the inductive and combined mode. As seen, lower frequencies (in the inductive or combined mode) are preferred so as to enable higher angular resolution.

C. *Tissue dielectric property variations*

Human tissue properties (permittivity, ε_r, and loss tangent, tanδ) vary from person to person and even from time to time for the same individual. The proposed system must be ideally insensitive to such changes in the underlying tissues. To explore the latter, tissue properties are varied by ±20% [31] from their nominal values (2/3 muscle in Fig. 2). Simulation results for characteristic frequencies in the combined (230 MHz) and inductive (34 MHz) mode are shown in Fig. 7(a) and Fig. 7(b), respectively. At 230 MHz, $|S_{21}|$ gets considerably impacted by changes in the underlying tissue properties. By contrast, at 34 MHz, $|S_{21}|$ is shown to be extremely robust to changes in the underlying tissues. That is, our results highlight remarkable advantages for the inductive mode. Notably, simulations for air medium used to replace the 2/3 muscle at 34 MHz also indicate an identical pattern to that of Fig. 7(b). This is a unique advantage for experimental testing purposes, implying that Styrofoam phantoms (e.g., Fig. 3), rather than tissue-emulating materials, can be employed to validate our sensor. The reason is that coils are inductively coupled via magnetic fields and are not radiating. Since human tissue has a relative permeability of $\mu_r \sim 1$, magnetic coupling is not affected by the presence or absence of tissue.

D. *Combined Effect and Optimal Frequency Selection*

For optimal frequency selection, the effect of all three aforementioned parameters needs to be taken into account. To ensure tolerance to tissue dielectric property variations as well

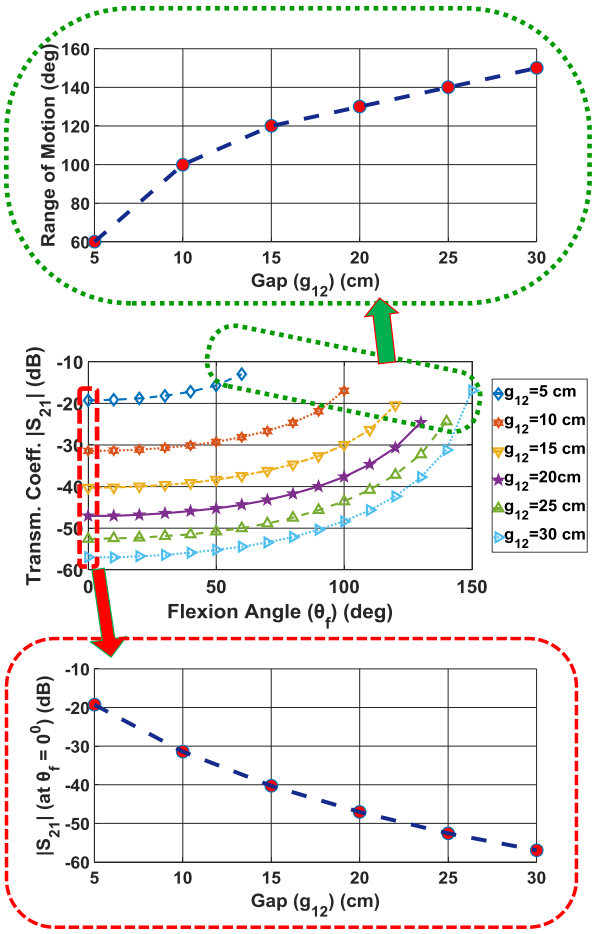

Fig. 9. $|S_{21}|$ as a function of flexion angle for various distances between the coils (g_{12}). Top inset depicts the trend of increase in range of motion with increasing g_{12}. Bottom inset depicts the trend of degradation in $|S_{21}|$ with increasing g_{12}.

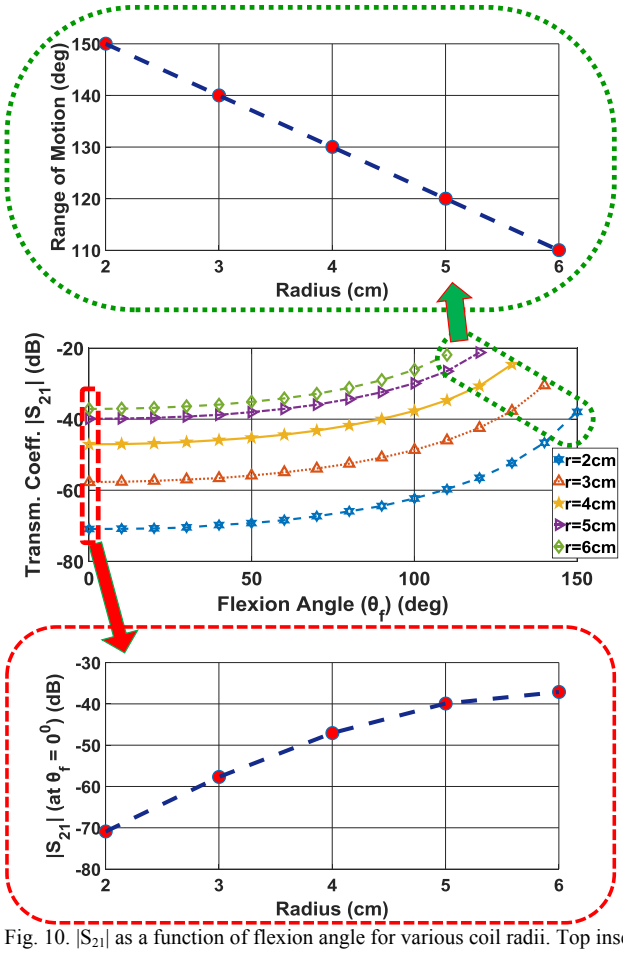

Fig. 10. $|S_{21}|$ as a function of flexion angle for various coil radii. Top inset depicts the trend of increase in range of motion as radius increases. Bottom inset depicts the trend of improvement in $|S_{21}|$ with increasing radius.

as high angular resolution, operation deep in the inductive mode is preferred. On the other hand, for reduced power requirements on the transmit side, higher frequencies in the inductive mode or even the combined mode are preferred. With this trade-off in mind, we herewith select the 34 MHz operating frequency.

VI. Experimental Validation

To validate our simulations, experiments are carried out using the set-up of Fig. 3. The optimal operation frequency of 34 MHz is selected, and coils are made resonant via a lumped capacitor per previous discussions. Simulation vs. experimental results at various coil gaps (g_{12} = 10, 15, 20 cm) are summarized in Fig. 8. As seen, excellent agreement is achieved. Even more importantly, e-thread coils perform identical to their copper counterparts while also being flexible and extremely robust to high/low temperatures, washing/drying, and mechanical duress [32].

To confirm the validity of the Styrofoam fixture in Fig. 3, experiments with ground beef phantom are also performed at g_{12} = 15 cm. Ground beef phantom has often been used in the literature to accurately emulate the average and frequency-dependent properties of the human body. In this case, average discrepancies vs. simulations for all flexion angles are smaller than 0.07 dB. That is, Styrofoam can indeed by employed as an alternative to tissue-emulating materials.

VII. Additional Considerations

A number of additional factors are hereafter explored, identified as crucial in designing, customizing, increasing the robustness, improving the performance, and ensuring the safety of the proposed system for joint flexion monitoring. The simulation set-up of Fig. 2 is considered along with resonant coils at 34 MHz.

A. Selection of Coil Gap (g_{12})

Selection of coil gap (g_{12} per Fig. 2 and Fig. 3(a)) is a variable design parameter that may be readily optimized per case. The effect of g_{12} on system performance is hereafter discussed with reference to Fig. 9 that plots $|S_{21}|$ vs. θ_f for various gaps between the Tx and Rx coils (5 to 30 cm). As seen, a similar one-to-one correlation is observed between $|S_{21}|$ and θ_f in all cases. That is, either configuration can be employed to monitor joint flexion. Nevertheless, a trade-off comes into play. Referring to the bottom inset of Fig. 9, decrease in g_{12} leads to non-linear increase of $|S_{21}|$, and hence lower power requirements. This is expected given the inverse relationship between magnetic field and gap between the coils. However, decrease in g_{12} concurrently reduces the range of

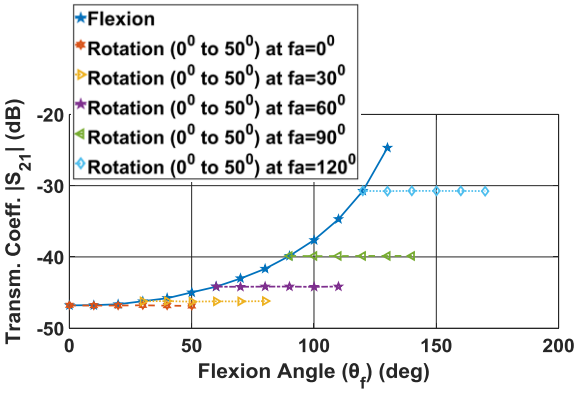

Fig. 11. $|S_{21}|$ as a function of flexion angle shown in solid line. Dotted lines show $|S_{21}|$ as a function of rotation angle at given flexion angles. Results highlight system robustness to limb rotation.

motion that can be captured by the coils; as g_{12} gets smaller, coils physically touch each other at smaller flexion angles. The trend is again non-linear and is better illustrated in the top inset of Fig. 9. As an example, for g_{12} = 5 cm, only angles in the 0^o to 60^o range can be captured. For g_{12} = 30 cm, the range expands all the way to 150^o, yet with a degradation in $|S_{21}|$ by as high as 38.8 dB, on average. That is, Fig. 9 provides design guidelines for optimal selection of g_{12} based on the application that the designer may have in hand (age of the individual, type of joint, power availability, receiver sensitivity, and so on).

B. *Effect of Limb Size*

Coil radius is directly determined by the underlying limb radius. It is, thus, expected that different coil radii will be employed for different individuals and/or different joints of the same individual. Along these lines, Fig. 10 demonstrates the effect of varying limb/coil radius (2 to 6 cm) upon the system performance. As expected, a similar one-to-one correlation is observed between $|S_{21}|$ and θ_f in all cases. That is, the proposed sensor is readily customizable. Nevertheless, system performance will be altered accordingly. Referring to the bottom inset of Fig. 10, increase in coil radius (viz. thicker limb) leads to non-linear increase of $|S_{21}|$, and hence lower power requirements. This is expected given the increase in flux linkage associated with increase coil radius. However, increase in coil radius concurrently reduces the range of motion that can be captured by the coils; as radius increases, coils physically touch each other at smaller flexion angles. The trend is illustrated in the top inset of Fig. 10. To sum up, the proposed approach is applicable to any limb size, with limb size impacting the system power requirements and range of motion, per Fig. 10. Of course, system design may be readily fine-tuned per application requirements by tweaking variable parameters, such as the coil gap depicted in Fig. 9.

C. *Robustness to Limb Rotation*

Limb rotation about its own axis (e.g., forearm pronation and supination), should not impact the flexion angle measurements. To validate the latter, rotation of the forearm about its own axis (from 0^0 to 50^0) is included in the model of Fig. 2. Simulation results are summarized in Fig. 11. Here, the

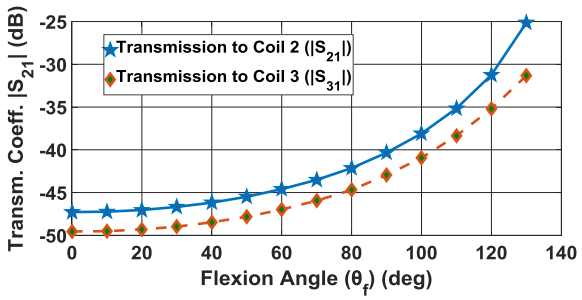

Fig. 12. Three-coil configuration with Coil 1 transmitting and Coils 2, 3 receiving: $|S_{21}|$ and $|S_{31}|$ values are plotted as a function of flexion angle.

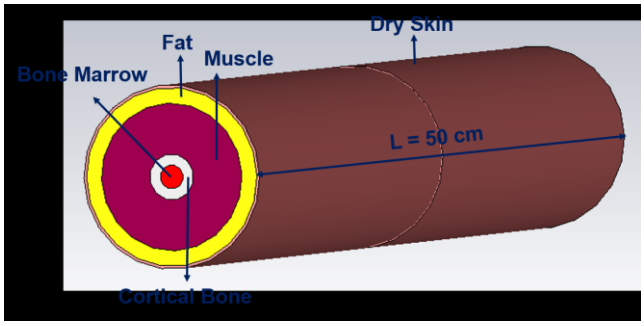

Fig. 13. Multi-tissue cylindrical model of human arm used for Specific Absorption Rate (SAR) calculations.

solid line plots $|S_{21}|$ as a function of flexion angle (θ_f), while the dotted lines plot $|S_{21}|$ as the forearm rotates at given flexion angles (θ_f = 0^o, 30^o, 60^o, 90^o, and 120^o). Remarkably, the captured $|S_{21}|$ value at any given flexion angle is not impacted by limb rotation. This is attributed to the inherent symmetry of the wrap-around coils, i.e., limb rotation does not change the flux linkage as there is no relative change in the area vector. Overall, this is a unique advantage of our joint flexion monitoring system that makes it extremely robust to rotation.

D. *Multi-Coil Configurations*

Referring to the real-world application of Fig. 1, consider a scenario where the Tx or Rx coil breaks down; the whole system will stop operating. Alternatively, consider an unforeseen scenario where error creeps in the measurement of the induced voltage at the Rx (e.g., Rx coil unwillingly shifts upon the garment); the measured flexion angles will be erroneous. To overcome such problems and increase system reliability/robustness, multi-coil configurations can be pursued. By adding multiple Tx and/or Rx coils, there is always a back-up in case of failure, while additional S-parameter data points are brought into play to statistically improve the measurement accuracy.

To prove the concept, the 3-coil set-up of Fig. 2 is employed, where Coil is transmitting and both Coil 2 and Coil 3 are receiving. In this example, g_{12} = 20 cm and g_{23} = 2 cm, per Fig. 2. Two sets of transmission coefficient values are recorded in this case, viz. $|S_{21}|$ and $|S_{31}|$, plotted in Fig. 12. As seen, both Rx coils can independently monitor flexion. Of course, more Tx and/or Rx coils can be added, per application requirements.

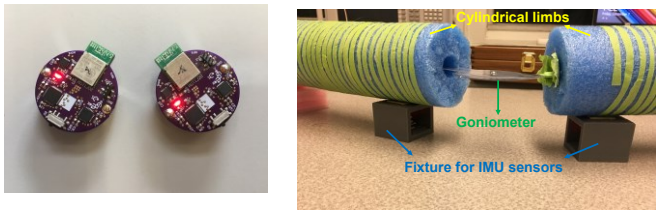

(a) (b)

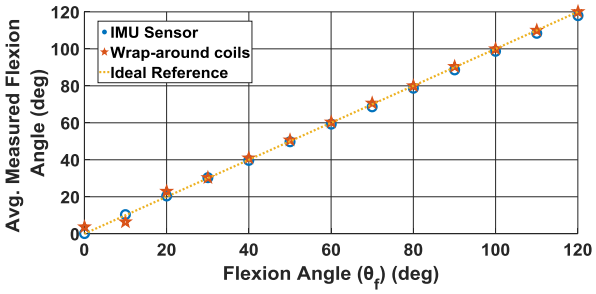

(c)

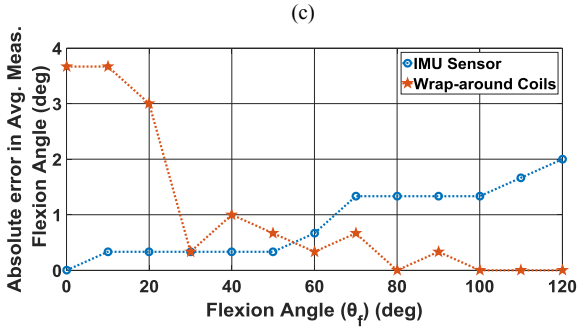

(d)

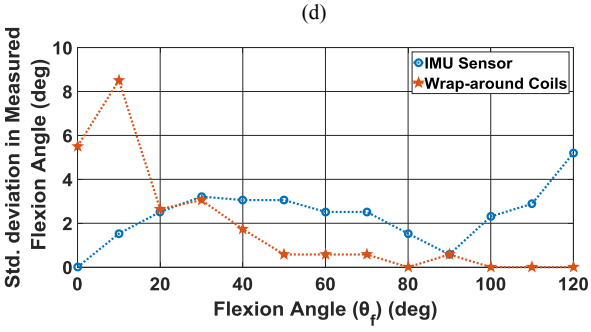

(e)

Fig. 14. (a) IMU sensors employed for benchmarking, (b) experimental set-up used to benchmark the wrap-around coils vs. IMUs, (c) flexion angle results averaged over three measurements, along with reference slope of 1, (d) absolute error vs. reference, and (e) standard deviation in measured flexion angle for three set of measurements.

E. Specific Absorption Rate

To ensure conformance with international safety guidelines, Specific Absorption Rate (SAR) studies are performed. To do so, the cylindrical arm model of Fig. 2 is considered, yet with a more realistic multi-tissue configuration depicted in Fig. 13. Specifically, skin, fat, muscle, cortical bone, and bone marrow tissues are employed, with thicknesses equal to, 1.17 mm, 6.63 mm, 21.45 mm, 4.68 mm and 5.07 mm, respectively. Thickness of the layers is obtained using the ratio calculated from the multi- layered model reported in [33]. Mass density values for each tissue are obtained from [34], and input power is set to -15 dBm (31.62 μW), as used to perform the experiments in Section VI. In this case, the maximum SAR value calculated over 1 g of tissue is equal to 3.98 μW/Kg, which is far less than the 1.6 W/kg maximum level allowed by the Federal Communications Commission (FCC). In fact, to hit the aforementioned FCC limit, our system's input power may be as high as 12.7 W. That is, the reported design is safe for human use.

F. Performance Benchmarking vs. State-of-the-Art IMUs

For performance benchmarking, a quantitative comparison is hereafter performed for the wrap-around coils vs. state-of-the-art IMUs (see Fig. 14(a)). The experimental set-up employs the cylindrical arm model of Fig. 3 and includes two 3D-printed fixtures to secure the IMUs and eliminate errors associated with relative rotation/shifting (see Fig. 14(b)). To translate the coil $|S_{21}|$ measurements into angles, a series of 7 measurements is performed, and the averaged results are used to create a reference map. The latter is eventually used to map $|S_{21}|$ measurements into flexion angles.

Flexion angles captured by both wrap-around coils and IMU sensors are shown in Fig. 14(c). Here, results are averaged over three independent measurements, with absolute errors from the reference angle values shown in Fig. 14(d) and standard deviation results shown in Fig. 14(e). As shown in Fig. 14(c), coils compare very well with the IMU sensors, and demonstrate a strong potential for flexion monitoring. Referring to Fig. 14(d), coils outperform IMUs at larger angles. In fact, the measurement error obtained from coils is less than 1^0 for flexion angles greater than 20^o. However, higher errors are observed at angles below 20^o, as attributed to the small range of $|S_{21}|$ values at low flexion angles (e.g., see Fig. 8). This will be explored further in future, as discussed in Section VIII. Referring to Fig. 14(e), reproducibility of coil measurements is again equivalent or better to that of IMUs at flexion angles beyond 20^o.

VIII. Conclusion

A new approach was introduced for seamlessly monitoring joint flexion using wrap-around coils, while being insensitive to relative rotation of the limb. Proof-of-concept simulation results were presented, validated by *in vitro* measurements, and further supplemented by discussions on design guidelines, and safety considerations. Contrary to state-of-the-art technologies used to monitor joint flexion, the reported approach: a) can be seamlessly integrated into garments for real-world monitoring, b) does not suffer from integration errors, c) does not require line-of-sight, and d) does not obstruct natural joint movement. Also, cost of the constituent sensor materials (e-threads or copper wire, connectors, and capacitors) is very low as compared to state-of-the-art IMUs or optical cameras. Even more importantly, the reported approach is extremely robust to changes in human tissue dielectric properties as verified via simulations in canonical models, and brings forward multiple degrees of freedom to optimize the design, per application requirements. Notably, quantitative comparison shows that this approach exhibits equivalent or superior performance vs. state-of-the-art IMUs, particularly for flexion angles greater than 20^o.

Future studies will focus on: a) further design optimization (e.g., multi-turn configurations), b) anatomical phantom models, c) *in vivo* experiments, d) elimination of bulky equipment, such as network analyzer, thereby making the set-up completely wireless, and e) improving the range of $|S_{21}|$ values at smaller angles to further improve accuracy and repeatability. Once fully optimized, this technology is envisioned to be employed as stand-alone and/or in combination with state-of-the-art technologies toward applications as diverse as rehabilitation, virtual reality, sports, and so on.

ACKNOWLEDGEMENT

The authors would like to thank Mr. Zeke Dalisky for his help with the IMU sensor experiments.

REFERENCES

[1] A. Salarian et al., "Ambulatory Monitoring of Physical Activities in Patients With Parkinson's Disease," in *IEEE Transactions on Biomedical Engineering*, vol. 54, no. 12, pp. 2296-2299, Dec. 2007.

[2] V. Bonnet et al., "Monitoring of hip and knee joint angles using a single inertial measurement unit during lower limb rehabilitation," *IEEE Sensors Journal*, vol. 16, no. 6, pp. 1557-1564, Mar. 2016.

[3] H. Wagner et al., "Upper-body kinematics in team-handball throw, tennis serve, and volleyball spike," *Scandinavian Journal of Medicine and Science in Sports*, vol. 24, no. 2, pp. 345-354, Apr. 2014.

[4] B.C. Heiderscheit et al., "Reliability and between-limb symmetry of joint kinetics and kinematics during a countermovement jump," *Medicine and Science in Sports and Exercise*, vol. 50, pp. 759, May 2018.

[5] T. P. Luu et al., "Gait adaptation to visual kinematic perturbations using a real-time closed-loop brain-computer interface to a virtual reality avatar," *Journal of Neural Engineering*, vol. 13, no. 3, Apr. 2016.

[6] Y. Xiao et al., "Human-robot interaction by understanding upper body gestures," *Presence: Teleoperators and Virtual Environments*, vol. 23, no. 2, pp. 133-154, 2014.

[7] M. Zhang et al., "Recent developments in game-based virtual reality educational laboratories using the Microsoft Kinect," *International Journal of Emerging Technologies in Learning*, vol. 13, no. 1, Jan. 2018.

[8] B. Birgit et al., "Body segment kinematics and energy expenditure in active videogames," *Games for Health Journal*, vol. 5, no. 3, Jun. 2016.

[9] M.C. Silaghi et al., "Local and global skeleton fitting techniques for optical motion capture," *International Workshop on Capture Techniques for Virtual Environments*, pp. 26-40, 1998.

[10] V.B. Zordan, and N.C. Van Der Horst, "Mapping optical motion capture data to skeletal motion using a physical model," *Eurographics Symposium on Computer Animation*, pp. 245-250, Jul. 2003.

[11] E. E. Stone and M. Skubic, "Unobtrusive, continuous, in-home gait measurement using the Microsoft Kinect," in *IEEE Transactions on Biomedical Engineering*, vol. 60, no. 10, pp. 2925-2932, Oct. 2013.

[12] F. Ferryanto and M. Nakashima, "Development of a markerless optical motion capture system for daily use of training in swimming," *Sports Engineering*, vol. 20, no. 1, pp. 63-72, Mar. 2017.

[13] M. El-Gohary and J. McNames, "Shoulder and elbow joint angle tracking with inertial sensors," in *IEEE Transactions on Biomedical Engineering*, vol. 59, no. 9, pp. 2635-2641, Sept. 2012.

[14] R. Kianifar et al., "Classification of squat quality with inertial measurement units in the single leg squat mobility test," *IEEE Engineering in Medicine and Biology Society*, Aug. 2016.

[15] B. Mariani et al., "On-Shoe Wearable Sensors for Gait and Turning Assessment of Patients With Parkinson's Disease," in *IEEE Transactions on Biomedical Engineering*, vol. 60, no. 1, pp. 155-158, Jan. 2013.

[16] C. Einsmann et al., "Modeling a wearable full-body motion capture system," *9th IEEE International Symposium on Wearable Computers*, Oct. 2005.

[17] S.C. Mukhopadhyah, "Wearable sensors for human activity monitoring: a review," *IEEE Sensors Journal*, vol. 15, no. 3, pp. 1321-1330, Mar. 2015.

[18] T. Shany et al., "Sensors-based wearable systems for monitoring of human movement and falls," *IEEE Sensors Journal*, vol. 12, no. 3, pp. 658-670, Mar. 2012.

[19] Y. Qi et al., "A novel approach to joint flexion/extension angles measurement based on wearable UWB radios," *IEEE Journal of Biomedical and Health Informatics*, vol. 18, no. 1, Jan. 2014.

[20] J.H.M. Bergmann et al., "An attachable clothing sensor system for measuring knee joint angles," *IEEE Sensors Journal*, vol. 13, no. 10, pp. 4090-4097, 2013.

[21] G. Moreton et al., "Investigation and characterization of a planar figure-of-eight coil as a curvature sensor," *2017 IEEE SENSORS*, Glasgow, 2017, pp. 1-3.

[22] Q. H. Abbasi, M. U. Rehman, K. Qaraqe, and A. Alomainy in *Advances in Body-Centric Wireless Communication: Applications and State-Of-The-Art* 1st ed. Institution of Engineering and Technology 2016.

[23] J. G. Santas et al., "Textile Antennas for On-Body Communications: Techniques and Properties," *The Second European Conference on Antennas and Propagation, EuCAP* 2007, Edinburgh, 2007, pp. 1-4.

[24] E. Moradi et al., "Effects of Sewing Pattern on the Performance of Embroidered Dipole-Type RFID Tag Antennas," in *IEEE Antennas and Wireless Propagation Letters*, vol. 11, pp. 1482-1485, 2012.

[25] T. Kaufmann et al., "Comparison of fabric and embroidered dipole antennas," 2013 *7th European Conference on Antennas and Propagation (EuCAP)*, Gothenburg, 2013, pp. 3252-3255.

[26] W.H. Hayt Jr., and J.A.Buck, "Time-Varying Fields and Maxwell's Equations" in *Engineering Electromagnetics 6th ed.,* Mc.Graw-Hill.

[27] C. Furse, D. A. Christensen, C. H. Durney, "Electric and Magnetic Fields: Basic Concepts," in *Basic Introduction to Bioelectromagnetics* 2nd ed., Boca Raton: CRC Press, 2009 pp. 30-34.

[28] P. Soontornpipit et al., "Design of implantable microstrip antenna for communication with medical implants," in *IEEE Transactions on Microwave Theory and Techniques*, vol. 52, no. 8, pp. 1944-1951, Aug. 2004.

[29] Syscom Advanced Materials. Available: http://www.metalcladfibers.com

[30] D. Means and K. Chan, "Evaluating compliance with FCC guidelines for human exposure to radiofrequency electromagnetic fields," OET Bulletin 65, vol. Supplement C, 2001.

[31] A. Kiourti, and K.S. Nikita, "Numerical assessment of the performance of a scalp- implantable antenna: Effects of head anatomy and dielectric parameters," in *Bioelectromagnetics*, vol. 34, no. 3, pp-167-179, 2013.

[32] J. Zhong et al., "Conformal Load-Bearing Spiral Antenna on Conductive Textile Threads," in *IEEE Antennas and Wireless Propagation Letters*, vol. 16, pp. 230-233, 2017.

[33] M. S. Wegmueller et al., "An Attempt to Model the Human Body as a Communication Channel," in *IEEE Transactions on Biomedical Engineering, vol*. 54, no. 10, pp. 1851-1857, Oct. 2007.

[34] Jaehoon Kim and Y. Rahmat-Samii, "Implanted antennas inside a human body: simulations, designs, and characterizations," in *IEEE Transactions on Microwave Theory and Techniques*, vol. 52, no. 8, pp. 1934-1943, Aug. 2004.